Spatial decoupling of dehydrogenation and CO oxidation by Ni-Co-Ti hierarchical trimetallic catalyst for electrocatalytic oxidation of methanol

Shenghao Zhao [a], Tianqi Wang [a], Zhijiao Ji [a], Yajun Song [a], Yi Li [a,b,c,*], Jia Liu [a,d,e,*], Wenping Hu [a,b,c]

[a] *Tianjin Key Laboratory of Molecular Optoelectronics, Department of Chemistry, School of Science, Tianjin University, Tianjin 300072, People's Republic of China*
[b] *Haihe Laboratory of Sustainable Chemical Transformations, Tianjin 300192, People's Republic of China*
[c] *Collaborative Innovation Center of Chemical Science and Engineering (Tianjin), Tianjin 300072, People's Republic of China*
[d] *Key Laboratory of Advanced Energy Materials Chemistry (Ministry of Education), College of Chemistry, Nankai University, Tianjin 300071, People's Republic of China*
[e] *Yulin University, Yulin 719000, Shanxi Province, People's Republic of China*

ARTICLE INFO

ABSTRACT

Methanol electro-oxidation reaction (MOR) is the kernel of methanol fuel cell. When the multi-step microscopic transformations process of MOR couples and occurs on the same active site, undoubtedly it reduces the probability of reaction and increases the steric hindrance, resulting in slow reaction kinetics and degradation of catalytic performance. In order to decouple the dehydrogenation and CO oxidation in MOR, herein we synthesized the hierarchical catalyst (NiCo/N-TiO$_2$ @NaOH) with bifunctional spatial distribution, which displayed 73 mA cm^{-2} at the potential of 1.5 V (vs. RHE) and only 20 % degradation of performance after continuously electrolysis over 40,000 s. Based on analysis of mass transfer and electron transport in hierarchical structure, combining with in-situ mass spectrometry and theory calculation, the high MOR performance of NiCo/N-TiO$_2$ can be ascribed to the spatial decoupling the MOR reactions including dehydrogenation under synergic effect of Ni/Co and CO oxidation on N-TiO$_2$ film.

1. Introduction

The electro-catalysts have played a gravel role in energy conversion over the decades because of the advantages of high efficiency and sustainable. Specially, direct methanol fuel cells (DMFCs) with excellent energy density, which is a device that can convert to electrical energy from chemical energy directly, have received extensive attention over the past several years [1–4]. The development of high efficient catalysts to improve methanol electrooxidation (MOR) dynamics is hot spot in this field. Therefore, precious metals are often used as the anode electrode, such as Pt [5] and Pd [6–8]. For improving the performance, the strategies of modifying nano-structure and adjusting morphology of precious metal for obtaining high active index facets are always employed. But the price of precious metals and the catalyst poisoning are still challenges for Pt-based electro-catalysts [9,10]. In sight of that, Ni-based catalysts, one of the non-precious metal catalysts, have been extensively discussed for MOR because of its high abundance, outstanding performances in alkaline media, and great surface oxidation

properties [11,12]. Recently, the research on Ni based catalysts mainly focuses on increasing the active sites by morphology regulation [13,14], accelerating the surface oxidation of Ni by doping [15], regulating the Ni orbital energy level by introducing vacancies [16,17], and improving the activity of catalytic sites by constructing synergistic structure [18, 19]. There are different advantages among them, in detail, morphology regulation can reveal more active sites, increasing electrochemically active surface area; doping, introducing vacancies and synergistic effect can precisely change the surrounding electronic environment of active species, increasing interaction between active species and substrates.

However, Ni based catalyst for MOR still has a great promotion space. The essence above effective strategies is the regulation of local electron environment and morphology of Ni, whose active only origin from modified Ni, resulting in the presence of challenge about service life of active species. Therefore the exploration of other new strategies also should be operated to extend service life and industrialization. The electrocatalytic oxidation process of methanol in alkaline solution can be simply decomposed into six processes, including four

dehydrogenation proton transfer processes, and the process of CO oxidation to CO_2 and final conversion to CO_3^{2-} [20]. In this complex conversion process, coupling of dehydrogenation and CO oxidation, CO cumulative adsorption and occupying by CO_3^{2-} on active sites result in a sluggish kinetics of MOR. Therefore, to accelerate MOR kinetics, dehydrogenation and CO oxidation must be decoupled and occur at different reaction sites. Because if CO oxidation occurs on the non-dehydrogenation active site, it does not only overcome low reaction collision probability but also alleviate CO poisoning and avoid the influence of CO_3^{2-} occupying on the activity. Therefore the hierarchical structure was proposed for better separation of the CO and CO_3^{2-} from Ni species in space.

Considering the spatial decoupling of MOR reaction, we design a reasonable spatial distribution of active sites for dehydrogenation and CO oxidation. Different from the simple relationship between catalytic active centers and supports, the different area should owe its special active center for specialized reaction. The design of hierarchical can ensure the quick separation of intermediate toxic substances and CO_3^{2-} from active sites of dehydrogenation, resulting in the active species of dehydrogenation can operate, efficiently and consistently. TiO_2, which has the advantages of low cost, excellent corrosion resistance in alkali solution similar to carbon based materials, facile controlling of morphology, is often used in various catalytic reaction scenarios, especially in photocatalysis [21]. Herein, TiO_2 is selected as the place for CO oxidation in MOR. The interaction between Ti-O on TiO_2 active surface can stabilize oxygen-containing groups such as·OH, so as to reduce the self-collision extinction of·OH radical and provide a large number of oxidation groups for CO oxidation. However, TiO_2 as a wide band gap semiconductor is not conducive to electron transmission. Therefore, it is necessary to modify it by doping hetero atoms and design in thin film structure to enhance the electron transmission ability and mass-transfer rate.

As aforementioned discussion, the hierarchical trimetallic catalyst was proposed for increasing amounts of metal sites and helping the complete migration of CO from active metal sites in limited space in this work. Simply stated, the modified TiO_2 film as CO oxidation active center was made by hydrothermal. Amounts of NiCo active metal site as dehydrogenation active center were prepared by electrodepositing with low cost and high effective on the TiO_2 film. On one hand, the catalyst performance of NiCo-decorated TiO_2 was focused, and the technological parameters were optimized for industrial application. What is more, the main intermediates produced in the MOR were investigated by in situ mass spectrometry and in situ electrochemical Raman spectroscopy. Density function theory (DFT) was also used for catalytic mechanism elucidation. Along with the understanding of catalytic mechanism of prepared materials, this research will also help expedite common use of DMFCs.

2. Experimental procedures

2.1. Reagents

All used reagents were belonged to analytical reagent grade in the work. Cobalt nitrate hexahydrate ($Co(NO_3)_2 0.6 H_2O$, 98 %), nickel nitrate hexahydrate ($Ni(NO_3)_2 0.6 H_2O$, 98 %), potassium chloride (KCl, 98 %) potassium hydroxide (KOH, 85 %), urea (CH_4N_2O, 97 %), and sodium hydroxide (NaOH, 97 %) were obtained from Aladdin Biochemical Technology Co. Ltd., Methanol (CH_3OH, 99 %), absolute ethanol (C_2H_5OH, 99.5 %), tetrabutyl titanate ($C_{16}H_{36}O_4Ti$, 98%), fuming nitric acid (HNO_3, 97 %) and acetone (C_3H_6O, 97 %) were obtained from Tianjin Damao Chemical Reagent Factory. Milli-Q water was provided by Tianjin University.

2.2. Procedures

2.2.1. Synthesis of N-TiO₂ film

The preparation of N-TiO_2 powder involved the following steps: The tetrabutyl titanate (3.4 mL) was dissolved in 15 mL absolute ethanol, which was designated as solution A. Then 120 mg urea was dissolved in the mixing solution which including 4 mL Milli-Q water, 4 mL absolute ethanol and 1 mL HNO_3, designated as solution B. The solution A dropped wise to the solution B under stirring, then stirred with continuous for 3 h. The resulting product was aged for several hours at a certain temperature, named as N-TiO_2 powder.

The prepared 200 mg N-TiO_2 powder was added into 5 mL NaOH solution (7 mol/L), the treated carbon paper (1×1.5 cm^{-2}) was placed into this mixed solution, which was dispersed using the ultrasonicator for 1 h. Then the mixing system was transferred into autoclave, which was heated and maintained 180 °C for 12 h. After naturally cooling, the products were removed from the autoclave and soaked in HCl question (0.1 M) for 1 h, then washed by Milli-Q water, repeatedly. After drying, the N-TiO_2 film was successfully prepared.

2.2.2. Synthesis of NiCo/N-TiO₂@NaOH

$Ni(NO_3)_2 0.6 H_2O$ (0.966 g), $Co(NO_3)_2 0.6 H_2O$ (0.483 g) and KCl (0.600 g) were mixed in 100 mL Milli-Q water. Electrodeposition was processed using carbon paper with N-TiO_2 film as working electrode by cyclic voltammetry (CV) at 50 mV s^{-1} for 10 cycles within − 0.4 to − 1.1 V (vs. Ag/AgCl), which was denoted as NiCo/N-TiO_2. Then the working electrode was treated in 0.10 M NaOH by CV (100 mV s^{-1}) between 0.1 and 0.7 V (vs. Ag/AgCl) with 10 cycles, which was denoted as NiCo/N-TiO_2 @NaOH.

2.3. Characterization

2.3.1. Material characterization

All morphology and structure of the materials were characterized by X-ray diffraction (XRD) patterns (RIGAKU SMARTLAB 9KW), field-emission scanning electron microscopy (FESEM) (SU8010, 10 kV). Transmission electron microscopy, High-Resolution TEM (HRTEM) and Energy Dispersive Spectrum (EDS) elemental mapping were measured on Tecnai G2 F20 (FEI America & Netherlands) operating at 200 kV. The surface composition and chemical state of materials were characterized from X-ray photoelectron spectroscopy (XPS) (ESCALAB 250xi). Elemental composition data of Ni and Co in the samples were determined by inductively coupled plasma mass spectrometry (ICP-MS, Agilent 7700x).

2.3.2. Electrochemical characterization

All electrochemical tests were carried out on CHI660E (Chenhua). The graphite electrode as the counter electrode, Hg/HgO as a reference electrode and the prepared electrode was used as working electrode. The electrocatalytic activity of materials was tested by linear sweep voltammetry (LSV) with 10 mV s^{-1}, corresponding Tafel curves and CV (50 mV s^{-1}). And the Tafel plots were fitted by the following equation: $\eta = b \log j + a$. In the question, η represents the overpotential, j represents the current density from LSV, b is the Tafel slope, a as the Tafel constant. Moreover, electrochemical impedance sepectroscopy (EIS) test was done in 100 kHz to 0.1 Hz, and the data was fitted by Zview program. The Electrochemical Active Surface Area (ECSA) of different electrodes were characterized via the double capacitance from CV at non-Faradaic potential region with different scanning rates, which can be calculated from the question, $ECSA = C_{dl}/C_s$, C_{dl} and C_s are electrochemical double layer capacitance and the specific capacitance of KOH solution (0.04 mF cm^{-2}), respectively [22].

3. Computational method

In DFT calculation, the geometry optimization was carried out by the

Generalized Gradient Approximation with the Perdew-Burke-Ernzerhof functional. The models of NiCo-OOH modified the (1 0 0) of NiOOH and N-TiO$_2$ modified by (1 0 1) of TiO$_2$ in $3 \times 3 \times 1$ super cells with a K-point of $1 \times 1 \times 1$ grid were used to identify the MOR activity sites. All surface models were built by including an additional vacuum region of 15 Å. The refined cell parameters of NiCo=OOH are a) 18.81 Å, b) 11.68 and c) 9.24 Å, and the refined cell parameters of N-TiO$_2$ are a) 30.62 Å, b) 11.33 Å and c) 15.40 Å. The Gibbs free energy change (ΔG) for elementary reaction was calculated from Nørskov's theory, the free energy of OH^- was calculated by $G(OH^-) = G(H_2O(l)) - G(H_2(g))/2$ [23]. We used a plane-wave energy cutoff of 450 eV. And we employed a gamma-centered Monkhorst k-point mesh of ($1 \times 1 \times 1$).

4. Results and discussion

4.1. The structure characterizations

The small nanoparticles were anchored on nitrogen doped TiO$_2$ film

(N-TiO$_2$) for higher mass-transfer rates of fluid, and the subsequent steps was illustrated in Fig. 1a. TiO$_2$ film containing nitrogen grown on the carbon paper was synthesized according to the traditional hydrothermal method, in which N-TiO$_2$ powder was as precursor, and metal particles were obtained by electrodeposition. The representative XRD diffraction peaks and Raman spectra of TiO$_2$ can be observed on the N-TiO$_2$ powder (Fig. S1). In particularly, Raman peaks broaden due to quantum size confinement effect, which indicated that nitrogen was doped in the lattice of TiO$_2$ [24,25]. After hydrothermal reaction, the micro appearance of obtained film on carbon paper was shown in Fig. 1b–d. The N-TiO$_2$ showed a large-area film structure (Fig. 1b), as if woven of much nanofibers. Fig. 1c also proved the presence of nanofibers. HRTEM image (Fig. 1d) expressly revealed that the lattice fringes spacing of about 0.35 nm indexed to the (101) plane for anatase phase TiO$_2$ [26, 27]. In fact, the slit structure of carbon paper was utilized in the growing process of film. More precisely, ultrasonic pretreatment was used to evacuate air from slit of carbon paper which was filled up immediately with alkali solution containing N-TiO$_2$ powder through an accelerated
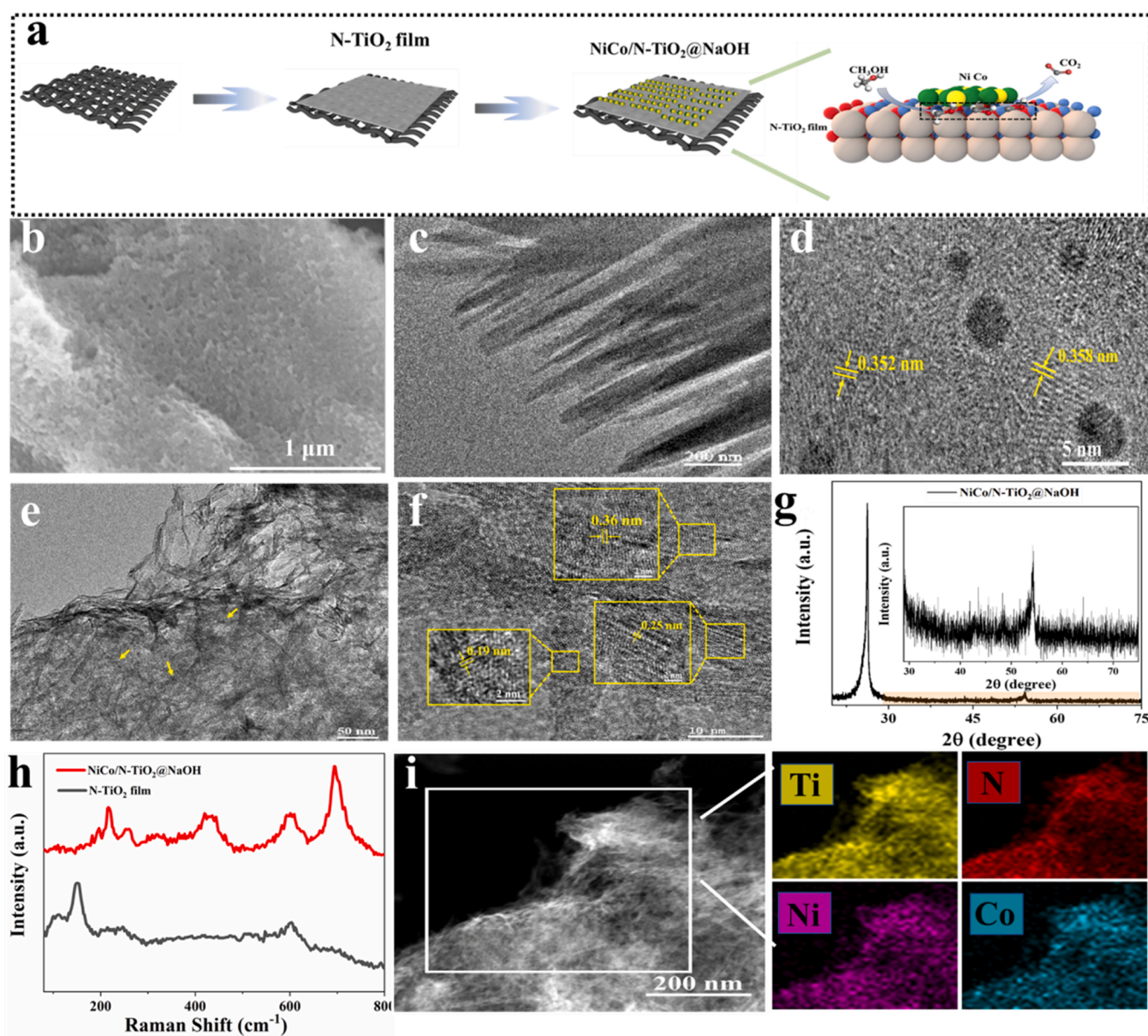

Fig. 1. (a) Fabrication of the NiCo/N-TiO$_2$ @NaOH. (b) SEM, (c) TEM, and (d) HRTEM of N-TiO$_2$ film. (e)TEM, (f) HRTEM, where the insert is an enlarged view, (g) XRD patterns, where the insert is an enlarged view around 28° and 75°, (h) Raman spectra, (i) EDS elemental mapping on N, Ti, Ni, Co of NiCo/N-TiO$_2$ @NaOH.

diffusion. Afterwards, hydrothermal treatment was carried out to boost preferential growth of nanofibers. With the increasing of synthesized time, titanate nanofibers grew and self-assembled into the film, and the interlacing structure of the carrier helped gaseous product diffuse. In addition, it can be concluded from Fig. S2 that the presence of N-TiO₂ film was beneficial to dispersion of the metal nanoparticles and improve deposition current efficiency. The metal particles were anchored on the N-TiO₂ film after electrodeposition, as displayed in Fig. 1e, the small metal particles (the diameter was from 1 nm to 8 nm) noted with arrows were relatively evenly dispersed on the film. Interestingly, the width of nanofibers was reduced after depositing metal due to the electrolysis of sodium hydroxide. The HRTEM image (Fig. 1f) showed the distances of the spaced lattice fringes were around 0.25 nm and 0.19 nm, corresponding to (101) and (110) planes of nickel cobalt hydroxide [28], and that of the anatase phase TiO₂ was also detected (0.36 nm). The diffraction peaks (38.9°,41.9°,60.3°) of XRD pattern (Fig. 1g) can be indexed as nickel-cobalt composite hydroxide (PDF#73–1520 and PDF#72–2280). And the difference of diffraction peaks was shows as shown in Fig. S3a after modifying carbon paper, suggesting that the composite was successfully prepared. Furthermore, the band around 706 cm⁻¹ attributes to the Ni-O, and the A1g vibration (around 460 cm⁻¹) mode in the Raman spectra (Fig. 1h) further indicated the formation of nickel cobalt hydroxides on the film [29–31]. In addition, the doping of nitrogen and uniform distribution of metal particles were further confirmed by EDS elemental mapping (Fig. 1i). It can be deduced the hierarchical trimetallic was successfully constructed, which is significance for high catalytic performance.

XPS was carried out to elucidate the effect of doping and electrolysis of sodium hydroxide on surface electronic states as well as chemical composition of materials. The spectrum of Ni 2p (Fig. 2a) can be mainly fitted into Ni 2p3/2 of 857 eV and Ni 2p1/2 of 873 eV with satellite bands at 863 eV and 880 eV [32,33]. Similarly, the fitting results of Co 2p spectrum (Fig. 2b) can be attributed to Co²⁺ accompanied with two peaks, corresponding to Co 2p3/2 (around 781.3 eV) and Co 2p1/2

(around 796.7 eV). Except for the above two peaks and corresponding satellite peaks, other peaks attributed to the bulk plasmons [34–36]. The decreased binding energy in Fig. 2a and b suggested complete conversion of metal hydroxide from oxides. Moreover, the O 1 s characteristic peaks indicated the presence of O-Ti, M-OH (M=Ni, Co), N-O-Ti and NOₓ species at 529 eV, 531 eV, 532 eV and 533 eV, respectively (Fig. 2c) [37]. The fitting of the Ti 2p XPS spectrum (Fig. 2d) showed the 2p3/2 ((459.1 eV)) and 2p1/2 ((464.5 eV)) peak of Ti⁴⁺, which result from spin–orbit splitting components. Fig. S3b displayed that nitrogen element was successfully doped, and the peaks were ascribed to N-O-Ti. The broad peak detected at around 400 eV, was resulted from the formation of N⁻ species [38,39]. Especially, the presence of O-Ti was beneficial to the adsorption and oxidation of CO because the increased activation of hydroxyl group (·OH) [40].

4.2. Electrochemical performance

The electrochemical property of all prepared catalysts was test by three-electrodes under the same conditions (Fig. S4). As shown in Fig. S4a and c, NiOOH or CoOOH from Ni²⁺ or Co²⁺ were formed during the first LSV scan and CV cycle. And the presence of N-TiO₂ film and electrolysis in sodium hydroxide solution cannot change the rate-determining step during oxygen evolution reaction (OER) by Tafel slope (Fig. S4b). Furthermore, the NiCo/N-TiO₂@NaOH had the largest double-layer capacitance (C_dl) (Figs. S4d and S5). In Fig. 3a and b, NiCo/N-TiO₂@NaOH led to maximum current density, around 73 mA cm⁻² at 1.5 V vs. RHE for MOR, which attributed the even distribution of increased metal particles and the presence of N-TiO₂ film. In Fig. 3d (from Fig. 3c), NiCo/N-TiO₂@NaOH displayed more favorable kinetics than other catalysts, proved by lower Tafel slope (59 mV dec⁻¹) which was related to the formation of NiOOH and mass transfer. The decreasing in Tafel slop represented the change of the rate-determining step.

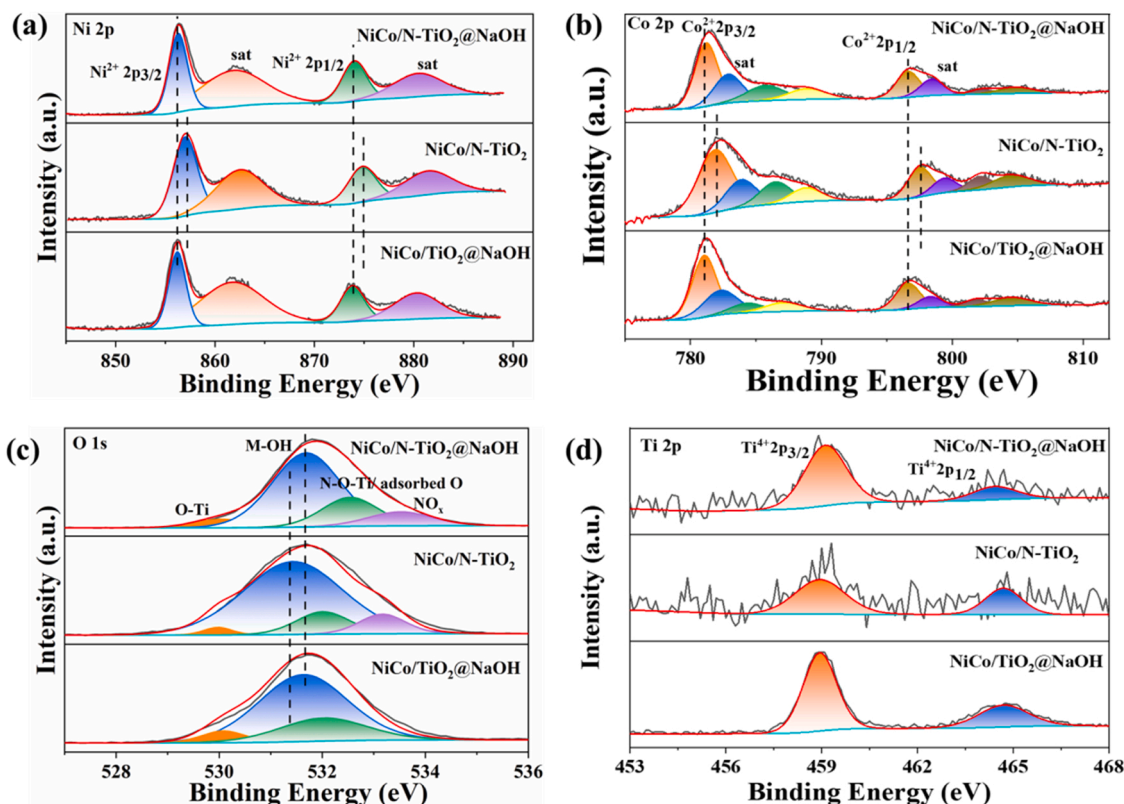It is very significant for electrochemical properties to estimate the

Fig. 2. (a) Ni 2p, (b) Co 2p, (c) O 1 s, and (d) Ti 2p for the XPS spectra of NiCo/TiO₂@NaOH, NiCo/N-TiO₂ and NiCo/N-TiO₂@NaOH.
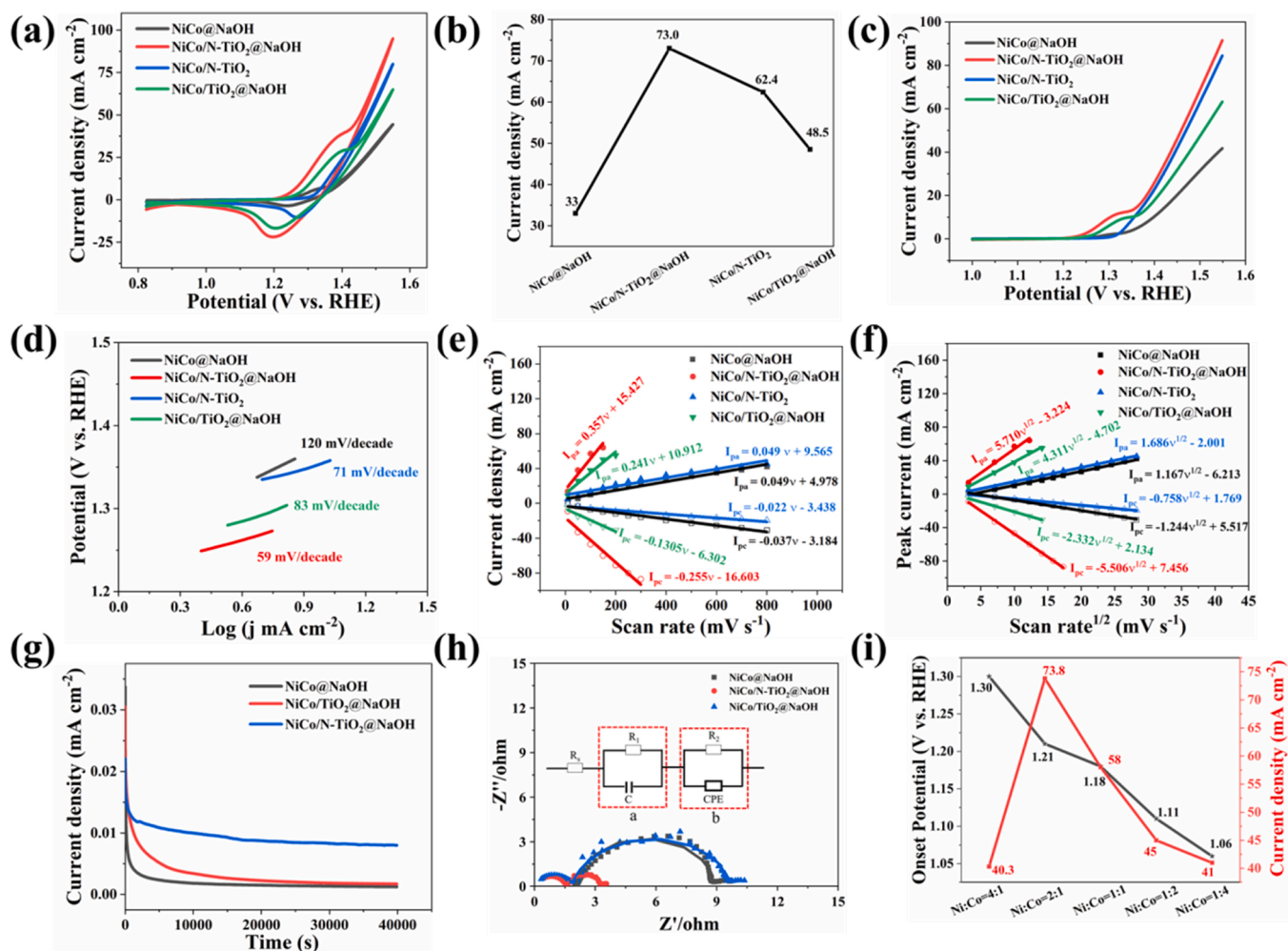
Fig. 3. (a) CV curves in 1 M KOH solution with 1 M methanol. (b) The current density at 1.5 V vs. RHE of different materials. (c) LSV curves, (d) the corresponding Tafel curves in 1 M KOH solution with 1 M methanol. (e) Linear fitting result of the peak current as a function of the scan rate. (f) Linear fitting result of the peak current as a function of the square root of scan rate. (g) Stability test curves for MOR at 1.4 V vs. RHE. (h) Nyquist curves, where the insert is the equivalent circuit. (i) The onset potential and current density of different ratio of metals at 1.5 V vs. RHE.

surface coverage of redox species (Γ^*) from the CV curves (Fig. S6). It can be estimated from the equation:

$$I_p = \left(\frac{n^2 F^2}{4RT}\right) \nu \Gamma^* \qquad (1)$$

where I_p is the anodic or cathodic peak current density, n represents the number of electrons, F is 96,845 C mol^{-1}, R is 8.314 J K^{-1} mol^{-1}, T is absolute temperature, ν as the scan rate [16]. Fig. 3e displayed the effect of scan rate on current, and the data point was less because the oxidation peak of metal coincides with the methanol oxidation peak at higher scan rate for certain catalysts. Averaging the results of cathodic and anodic, Γ^* of NiCo/N-TiO$_2$ @NaOH was 3.201×10^{-7} mol cm^{-2}, larger than that of NiCo@NaOH (4.499×10^{-8} mol cm^{-2}), NiCo/N-TiO$_2$ (4.498×10^{-8} mol cm^{-2}) and NiCo/TiO$_2$ @NaOH (1.942×10^{-7} mol cm^{-2}). What is more, the Γ^* of NiCo/N-TiO$_2$ @NaOH was larger than those reported previously for CoNi-decorated graphene (3.05×10^{-7} mol cm^{-2}) [41]. In addition, the peak of oxidation and reduction shifted positively and negatively (Fig. S6), respectively, which is attributed to electrochemical polarization.

The proton diffusivity (D) usually represents the rate-determining step where the formation of NiOOH from Ni(OH)$_2$. So the D was calculated for further research in the electrochemical by the Randles-Sevcik equation, as shown in the following question,

$$I_p = 2.69 \quad \times 10^5 n^{3/2} D^{1/2} C \nu^{1/2} \qquad (2)$$

In the equation, C is the initial concentration of redox species, which is assumed to be the proton concentration because of the reaction: $Ni(OH)_2 \rightarrow NiOOH + H^+$. The fitting results from Fig. S6 was shown in Fig. 3f, the linear function inferred a diffusion-limited redox reaction, which indicated high activity of the introduced electro-catalyst. And the specific D value of NiCo/N-TiO$_2$ @NaOH was 9.703×10^{-9} cm^2 s^{-1}, which indicated that a much faster diffusion of the limiting specie, comparing with that of other catalysts. Specially, NiCo@NaOH (4.602×10^{-10} cm^2 s^{-1}), NiCo/N-TiO$_2$ (5.405×10^{-10} cm^2 s^{-1}), NiCo/TiO$_2$ @NaOH (2.939×10^{-9} cm^2 s^{-1}).

The stability tests were carried out and shown in Fig. 3g. The current obviously reduced at time progress, and then remained relatively stable for all subjects, which can be attributed that the process of mass transfer diffusion and formation of intermediate. In detail, the fast kinetic of the reaction in the initial stage results in a dramatic decrease of adsorbed methanol molecules on the active sites. The presence of concentration difference causes the rate controlling step changing from electrochemical reaction to mass transfer diffusion between electrode surface and electrolyte. Therefore, the current density showed the sharp decrease in the initial stage. Along with the reaction proceed; the active sites were occupied by the intermediate, while the adsorption of methanol molecules is up to the liberation of the electrocatalytic sites.

Therefore, the number of methanol molecules adsorbed on active sites decreased, resulting in the slightly decrease of current density. The figure showed that the current decreased stage of NiCo/N-TiO$_2$ @NaOH was considerably shorter than that of others, indicating that rapid oxidation of intermediate products. The chronoamperometry displayed the nice stability of NiCo/N-TiO$_2$ @NaOH, which can continue to operate for 40,000 s. In addition, almost no metal shed by determining the metal contents (Ni and Co) in electrolyte after carrying for 40,000 s by ICP-MS, which was close to that of initial electrolyte (0.02 wt%).

To further reveal the electrode kinetics of the studied catalysts, the EIS was carried out at 1.4 V vs. RHE. Additionally, this method can evaluate the value of equivalent electronic device (such as capacitive and electrical conductivity). The Nyquist curves for all subjects were displayed in Fig. 3h, and the insert was the equivalent circuit. The obtained data points were superimposed with the fitting results, suggesting the equivalent circuit is reasonable. There was only an arc in the low frequency region for NiCo@NaOH, which indicated that the arc detected is in high frequency region because of the TiO$_2$ film. The difficulty of mass transfer between the electrode surface and the solution was increased after introducing the film, which was equal to R$_1$ of the equivalent circuit. The arc of high frequency region represented the resistance of charge transfer, which was equal to R$_2$ of equivalent circuit.

In addition, R$_s$ represented the solution resistance in equivalent circuit [42,43]. The fitting results as shown in Table S1, which displayed that the application of TiO$_2$ film increased R$_1$ and R$_2$, whereas the resistances of them were decreased after doping nitrogen. Therefore, NiCo/N-TiO$_2$ @NaOH exhibited the excellent electrochemical performance in Fig. 3b.

Fig. 3i displays the effect of metal content ratio on onset potential and current for MOR. The results suggested the onset potential decreased when the content of Co increased to a certain proportion, indicating there is cooperation role of metal in MOR. The optimal molar ratio of Ni and Co was 2:1. Based on the above result, it can be concluded that the quantum of nitrogen and ratio of metal have great effect on the catalyst performance of NiCo/N-TiO$_2$ @NaOH. Besides, the thickness and roughness of the film can indirectly influence on the catalyst performance too. Therefore, the parameters of hydrothermal time and concentration of NaOH in the synthesis process were optimized by evaluating the MOR electrocatalytic performance of obtained materials. As shown in Figs. S7–S9, the optimum catalysts were obtained under hydrothermal condition for 12 h with 7 M of NaOH. The comparison of the MOR catalytic performance among NiCo/N-TiO$_2$ @NaOH and other reported non-precious metal catalysts was summarized in Tables S2. It was considerable to note that the prepared catalyst clearly outperforms the other existing MOR non-precious metal catalysts.
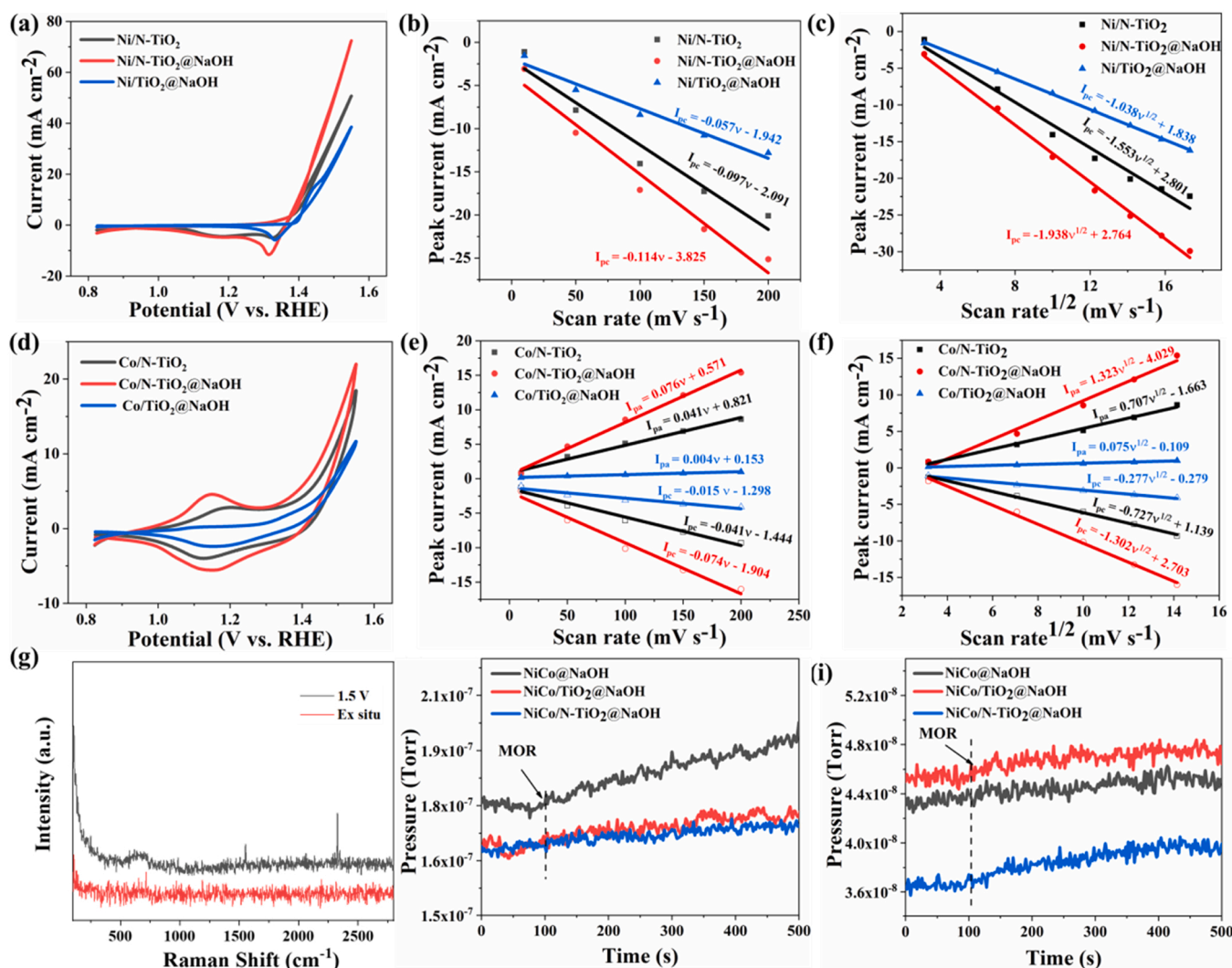

Fig. 4. (a) CV curves, (b) corresponding linear fitting of the cathodic current peak current as function of scan rate, and (c) linear fitting of the cathodic current peak current as function of the square root of scan rate of Ni-based catalysts. (d) CV curves, (e) corresponding linear fitting of the peak current as function of the scan rate, and (f) linear fitting of the peak current as function of the square root of scan rate of Co-based catalysts. (g) In situ electrochemical Raman spectroscopy of MOR on NiCo/N-TiO$_2$ @NaOH electrodes. (h) CO, (i) CO$_2$ of mass spectrometry for periodic measurement of during MOR at 1.5 V vs. RHE.

4.3. Reaction mechanism

In order to better understand the reasons why the NiCo/N-TiO$_2$ @NaOH exhibit higher catalytic activity for MOR and verify whether the reaction is decoupled, we conduct mechanism study. First, the single N-TiO$_2$ film has little catalytic activity for MOR (Fig. S10a), indicate that the initial reaction of dehydrogenation should occur on Ni/Co sites. Thus the catalyst performance of Ni-based and Co-based catalysts was respectively investigated for revealing the cooperation effect and catalytic mechanisms during MOR of NiCo/N-TiO$_2$ @NaOH. As shown in Fig. S11 the binding energy of Ni and Co was reduced by around 0.4 eV after electrolysis of sodium hydroxide, which was consistent with previous results (Fig. 2). Comparing Fig. 4a with d, the current density of Ni-based catalysts was significantly greater than that of Co-based catalysts, and the current density decreased with increasing the amount of Co within a certain range (Fig. S7), which indicated that Ni was the major active sites, and Co was the co-catalyst. Fig. 4b and c obtained from Fig. S12 displayed the fitting results of cathodic current peak current as function of the scan rate and square root of it for Ni-based catalysts, respectively. The calculated Γ^* and D were shown in Table S3, which can analyze the influence factors of the conformation of NiOOH in detail. The higher value of Γ^* means much more active sites of NiOOH. The larger value of D means faster formation of NiOOH. Compared Ni/N-TiO$_2$ @NaOH and NiCo/N-TiO$_2$ @NaOH, the result showed that the presence of Co was beneficial to the formation of NiOOH. Fig. 4d displayed two reduction peaks represents the formation of Co^{4+} in MOR, however, the reduction peak of Co^{4+} disappeared in the presence of Ni (Fig. 3a), because the electrons of Ni^{2+} transfer to Co^{4+} which prevent further oxidation of Co^{3+}. The electrons transfer form Ni to Co results in a rapid formation of NiOOH. Fig. 4e, f (from Fig. S12) displayed the fitting results of cathodic current peak current as a function of the scan rate and the square root of scan rate of Co-based catalysts, respectively. Compared with the Γ^* and D of NiCo/N-TiO$_2$ @NaOH, that of Co-based catalysts were so small which can be neglected (Table S3). With regard to Ni-based catalysts, the increasing of surface coverage in limited Ni species (Γ^*) was concerned with the doping of nitrogen, because of the higher efficiency of eletrodeposition. The improved proton diffusivity (D) related to the electrolysis of sodium hydroxide and introduction of Co. Therefore, there is obvious cooperation effect between Ni and Co, the presence of Co facilitates formation of NiOOH [44,45]. Based on above analysis, it can be concluded that the presence of Co accelerate the oxidation of nickel, simultaneously the initial step of MOR, dehydrogenation, take place on Ni^{3+} sites of NiOOH.

To investigate the following reaction pathway after dehydrogenation, the in situ electrochemical Raman spectroscopy was carried out for capturing intermediate products. The MOR on NiCo/N-TiO$_2$ @NaOH electrodes was performed in a custom-made cell filled with 1 M KOH solution with 1 M methanol, meanwhile, the Raman spectroscopy was applied. As shown in Fig. 4g, some peaks of material were observed between 500 and 700 cm^{-1} at the potential of 1.5 V. Besides the peaks of free CO$_2$ (around 2300 cm^{-1}) [46], the weak peak at around 1500 cm^{-1} was also observed, which is assigned to *COOH also proved by ^{1}H NMR (Fig. S13) [47,48]. It is worth noting that the peak of CO is absence, while *COOH is the intermediate compound of the oxidation of CO, which indicate that the material we prepared can rapidly oxidize CO.
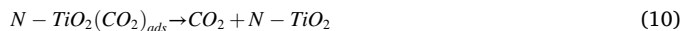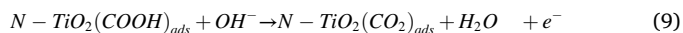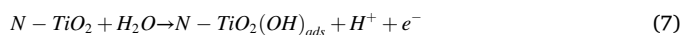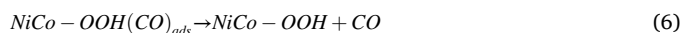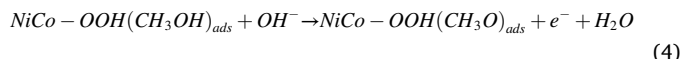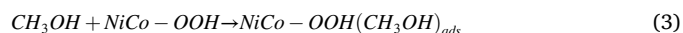
The gaseous products of MOR (CO and CO$_2$) were also monitored by mass spectrometry under certain potential to further illustrate the active site of CO oxidation. Fig. 4h and i displayed the composition change of CO and CO$_2$ in a MOR process, respectively. Combining with the results shown in Fig. S14, for the catalysts containing TiO$_2$ film, the relative content of CO in gas product did not change obviously, while that of CO$_2$ increased greatly in the MOR process. It suggested that CO oxidation probably occur on TiO$_2$ film, and the TiO$_2$ and N-TiO$_2$ film help the oxidation of CO, thus enhance the electrocatalytic performance for oxidation of methanol.

In addition, the CO poisoning tests further indicated the TiO$_2$ film indeed promotes CO oxidation. (Fig. S15). It can be seen from the current density of materials containing TiO$_2$ film decreased only around 24.6 % after introducing CO for 1200 s, which was much better than that without TiO$_2$ (decreased over 53.8 %).

In addition, CO$_2$ can convert to CO$_3^{2-}$ in KOH solution which may decrease the catalyst performance of NiCo/N-TiO$_2$ @NaOH after longer working. Therefore, the catalyst performance of target catalyst was tested after immersing in 0.5 M K$_2$CO$_3$ for 12 h. As shown in Fig. S16, the MOR performance significantly reduced after immersing in 0.5 M K$_2$CO$_3$. In comparison, the OER current density increased after immersing anode in K$_2$CO$_3$ solution (Fig. S17a and b). The catalyst after immersing in K$_2$CO$_3$ solution has a higher reaction kinetic rather than high ECSA (Fig. S17c–e). It can be indicated that the active of active metals was not decreased by the adsorption of K$_2$CO$_3$. In addition, the Tafel slope (89 mV dec^{-1}) was still smaller than 120 mV dec^{-1}, indicating the MOR reaction can happen at certain potential, and the initial reaction rate was higher. In other words, active Ni still exposed CO oxidation step turned to the rate determining step. Therefore, it can conclude that the CO$_3^{2-}$ occupy the surface of N-TiO$_2$ film decreasing kinetics of MOR, which suggest the introducing of N-TiO$_2$ film can not only help CO oxidation, but also adsorb CO$_3^{2-}$ converted from CO$_2$. The effected spatial decoupling between toxic substance and active sites was successfully achieved in NiCo/N-TiO$_2$ @NaOH.

Therefore, we deduced that Ni-Co-Ti hierarchical trimetallic (Ni, Co, and N-TiO$_2$ film) constitute the active sites of the catalyst (NiCo/N-TiO$_2$ @NaOH) in the process of MOR. In detail, Ni is the major active sites, Co is the co-catalyst, and N-TiO$_2$ film can not only help the deposition of metal, but also engage in oxidation of CO as well as adsorption of CO$_3^{2-}$, so that the service life is prolonged. Therefore, the mechanism for the oxidation of methanol in NiCo/N-TiO$_2$ @NaOH mainly involves dehydrogenation of methanol on NiCo-OOH (3−6), and oxidation of CO on the surface of N-TiO$_2$ film (7−10).

$$CH_3OH + NiCo - OOH \rightarrow NiCo - OOH(CH_3OH)_{ads} \tag{3}$$

$$NiCo - OOH(CH_3OH)_{ads} + OH^- \rightarrow NiCo - OOH(CH_3O)_{ads} + e^- + H_2O \tag{4}$$

$$NiCo - OOH(CH_3O)_{ads} + 3OH^- \rightarrow NiCo - OOH(CO)_{ads} + 3e^- + 3H_2O \tag{5}$$

$$NiCo - OOH(CO)_{ads} \rightarrow NiCo - OOH + CO \tag{6}$$

$$N - TiO_2 + H_2O \rightarrow N - TiO_2(OH)_{ads} + H^+ + e^- \tag{7}$$

$$CO + N - TiO_2(OH)_{ads} \rightarrow N - TiO_2(COOH)_{ads} \tag{8}$$

$$N - TiO_2(COOH)_{ads} + OH^- \rightarrow N - TiO_2(CO_2)_{ads} + H_2O + e^- \tag{9}$$

$$N - TiO_2(CO_2)_{ads} \rightarrow CO_2 + N - TiO_2 \tag{10}$$

To give deep insight into the important effect of N-TiO$_2$ film, the Gibbs free energy change (ΔG) based on the elementary reaction was calculated by DFT. Fig. S10b displayed that co-deposition of Ni, Co was better catalytic properties, indicating the absence of NiOOH-CoOOH interface. The calculation models of NiCo-OOH and N-TiO$_2$ as shown in Fig. S18. The reaction mechanism and the electron transfer pathway on NiCo/N-TiO$_2$ @NaOH were displayed in Fig. 5a. The dehydrogenation occurs on the surface of NiCo-OH, alternatively, CO was oxidized on the surface of N-TiO$_2$ film with hydroxyl radicals. For the dehydrogenation reaction (Fig. 5b), the potential determining step was changed after doping Co from CH$_3$OH* → CH$_3$O* to CH$_3$O* → CH$_2$O*, and the max ΔG is reduced by 1.45 eV, which is in agreement with the results of Tafel slope. The introduction of Co is beneficial for dehydrogenation of MOR. Fig. 5d displayed the ΔG of CO oxidation on the NiCo-OOH and N-TiO$_2$, suggesting an endothermic process, and the max ΔG is 3.49 eV (CO$_2$* → CO$_2$). But every elementary reaction is exothermic reaction from CO to CO$_2$ on N-TiO$_2$, further indicating N-TiO$_2$ is the
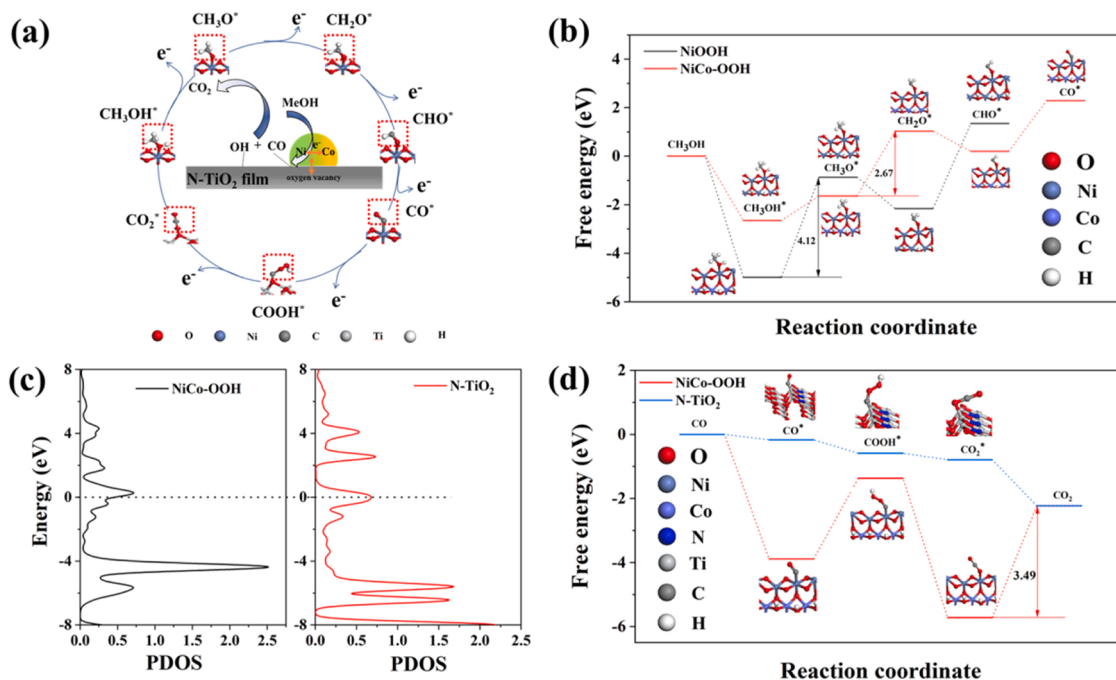
Fig. 5. (a) Schematic of electron transfer of MOR for NiCo/N-TiO$_2$ @NaOH. (b) ΔG for methanol oxidation to CO. (c) PDOS of O s orbital of·OH adsorbed on NiCo-OOH and N-TiO$_2$. (d) ΔG for CO to CO$_2$.

reaction active site for CO oxidation. What's more, the ΔG of formation of·OH from H$_2$O on NiCo-OOH is larger than that of N-TiO$_2$ surface (Fig. S19), indicating that·OH prefer to form on the N-TiO$_2$ film. And PDOS of O in·OH adsorbed on NiCo-OOH is smaller than that of N-TiO$_2$ at the Fermi level (Fig. 5c), suggesting it is easier to form COOH from CO on N- TiO$_2$.

5. Conclusion

In summary, taking the migration and oxidation of intermediates in MOR as the breakthrough point, the hierarchical trimetallic catalyst (NiCo/N-TiO$_2$ @NaOH) with spatial decoupling function was prepared. Mass and electron transport in hierarchical structure were discussed by series characterizations. N-TiO$_2$ film helped the deposition of metals and oxidation of CO, and the evenly dispersed small metal particles on the N-TiO$_2$ film provided abundant active sites for the dehydrogenase of CH$_3$OH. The optimal sample can work continuously for 40,000 s. The introduction of Co accelerates formation of NiOOH which is main active sites for dehydrogenation, which were beneficial to MOR. Therefore, NiCo/N-TiO$_2$ @NaOH has the larger Γ^*(3.201 $\times$ 10^{-7} mol cm^{-2}) and D (9.703 $\times$ 10^{-9} cm^2 s^{-1}) than those reported previously. In addition, the presence of N-TiO$_2$ film can provide abundant·OH to capture and oxidize CO, effectively alleviating catalyst poisoning. The effected spatial decoupling between toxic substance and active sites enhances the catalytic performance of the catalyst and prolong the lifetime of active metals. This work not only prepares an inexpensive, higher performance catalyst for MOR, but also proposes the spatial decoupling strategy which provides a new design idea for designing new catalysts with excellent activity and stability.

CRedit authorship contribution statement

The manuscript was written through contributions of all authors. All authors have given approval to the final version of the manuscript.

Declaration of Competing Interest

The authors declare that they have no known competing financial interests or personal relationships that could have appeared to influence the work reported in this paper.

Data availability

Data will be made available on request.

Appendix A. Supporting information

Supplementary data associated with this article can be found in the online version at doi:10.1016/j.apcatb.2022.122024.

References

[1] K. Zhang, C. Wang, H. You, B. Zou, S. Guo, S. Li, Y. Du, Advanced Plasmon-driven ethylene glycol oxidation over 3D ultrathin Lotus-like PdCu nanosheets, Chem. Eng. J. 438 (2022) 135666–135675.

[2] J. Yang, R. Hübner, J. Zhang, H. Wan, Y. Zheng, H. Wang, H. Qi, L. He, Y. Li, A. A. Dubale, A robust PtNi nanoframe/N-doped graphene aerogel electrocatalyst with both high activity and stability, Angew. Chem., Int. Ed. 133 (2021) 9676–9683.

[3] B.Y. Xia, H.B. Wu, X. Wang, X.W. Lou, One-pot synthesis of cubic PtCu$_3$ nanocages with enhanced electrocatalytic activity for the methanol oxidation reaction, J. Am. Chem. Soc. 134 (2012) 13934–13937.

[4] G. Zhu, Y. Zhao, L. Su, P. Qiu, W. Luo, Recent advances on the synthesis of mesoporous metals for electrocatalytic methanol oxidation, Emergent. Mater 3 (2020) 291–306.

[5] J. Li, C. Wang, H. Shang, Y. Wang, H. You, H. Xu, Y. Du, Metal-modified PtTe$_2$ nanorods: surface reconstruction for efficient methanol oxidation electrocatalysis, Chem. Eng. J. 424 (2021) 130319–130327.

[6] N. Yang, D. Chen, P. Cui, T. Lu, H. Liu, C. Hu, L. Xu, J. Yang, Heterogeneous nanocomposites consisting of Pt$_3$Co alloy particles and CoP$_2$ nanorods towards high-efficiency methanol electro-oxidation, SmartMat 2 (2021) 234–245.

[7] C. Yuan, H. Gao, Q. Xu, X. Song, C. Zhai, M. Zhu, Pt decorated 2D/3D heterostructure of Bi$_2$WO$_6$ nanosheet/Cu$_2$S snowflake for improving electrocatalytic methanol oxidation with visible-light assistance, Appl. Surf. Sci. 521 (2020) 146431–146440.

[8] K. Zhang, T. Song, C. Wang, H. You, B. Zou, S. Guo, Y. Du, S. Li, Surface plasmon resonance boost electrocatalytic alcohol oxidation over three-dimensional PdM (M= Au, Ag, Cu) nanosheet assemblies, Inorg. Chem. 60 (2021) 7527–7535.

[9] N. Tian, Z.Y. Zhou, S.G. Sun, Y. Ding, Z.L. Wang, Synthesis of tetrahexahedral platinum nanocrystals with high-index facets and high electro-oxidation activity, Science 316 (2007) 732–735.

[10] Y. Jin, Z. Zhang, H. Yang, P. Wang, C. Shen, T. Cheng, X. Huang, Q. Shao, Boosting hydrogen production with ultralow working voltage by selenium vacancy enhanced ultrafine platinum nickel nanowires, SmartMat 3 (2022) 130–141.

[11] Q. Yi, W. Huang, J. Zhang, X. Liu, L. Li, Methanol oxidation on titanium-supported nano-scale Ni flakes, Catal. Commun. 9 (2008) 2053–2058.

[12] C. Wang, H. Shang, H. Xu, Y. Du, Nanoboxes endow non-noble-metal-based electrocatalysts with high efficiency for overall water splitting, J. Mater. Chem. A 9 (2021) 857–874.

[13] M.A. Kamyabi, K. Ebrahimi-Qaratapeh, M. Moharramnezhad, Silica template as a morphology-controlling agent for deposition of platinum nanostructure on 3D-Ni-foam and its superior electrocatalytic performance towards methanol oxidation, J. Porous Mater. 28 (2021) 393–405.

[14] T. Wang, X. Cao, L. Jiao, Ni$_2$P/NiMoP heterostructure as a bifunctional electrocatalyst for energy-saving hydrogen production, eScience 1 (2021) 69–74.

[15] J. Li, C. Xing, Y. Zhang, T. Zhang, M.C. Spadaro, Q. Wu, Y. Yi, S. He, J. Llorca, J. Arbiol, Nickel iron diselenide for highly efficient and selective electrocatalytic conversion of methanol to formate, Small 17 (2021) 2006623–2006634.

[16] W. Yang, X. Yang, J. Jia, C. Hou, H. Gao, Y. Mao, C. Wang, J. Lin, X. Luo, Oxygen vacancies confined in ultrathin nickel oxide nanosheets for enhanced electrocatalytic methanol oxidation, Appl. Catal. B 244 (2019) 1096–1102.

[17] C. Zheng, X. Zhang, Z. Zhou, A first-principles study on the electrochemical reaction activity of 3d transition metal single-atom catalysts in nitrogen-doped graphene: Trends and hints, eScience 2 (2022) 219–226.

[18] M. Asgari, M.G. Maragheh, R. Davarkhah, E. Lohrasbi, A.N. Golikand, Electrocatalytic oxidation of methanol on the nickel–cobalt modified glassy carbon electrode in alkaline medium, Electrochim. Acta 59 (2012) 284–289.

[19] H. Lei, Q. Zhang, In situ electrochemical redox tuning of Pd-Co hybrid electrocatalysts for high-performance methanol oxidation: strong metal-support interaction, J. Colloid Interface Sci. 588 (2021) 476–484.

[20] F. Meng, C. Dai, Z. Liu, S. Luo, J. Ge, Y. Duan, G. Chen, C. Wei, R.R. Chen, J. Wang, Methanol electro-oxidation to formate on iron-substituted lanthanum cobaltite perovskite oxides, eScience 2 (2022) 87–94.

[21] M. Tian, G. Wu, A. Chen, Unique electrochemical catalytic behavior of Pt nanoparticles deposited on TiO$_2$ nanotubes, ACS Catal. 2 (2012) 425–432.

[22] N. Wu, M. Zhai, F. Chen, X. Zhang, R. Guo, T. Hu, M. Ma, Nickel nanocrystal/ nitrogen-doped carbon composites as efficient and carbon monoxide-resistant electrocatalysts for methanol oxidation reactions, Nanoscale 12 (2020) 21687–21694.

[23] J.K. Nørskov, J. Rossmeisl, A. Logadottir, L. Lindqvist, J.R. Kitchin, T. Bligaard, H. Jonsson, Origin of the overpotential for oxygen reduction at a fuel-cell cathode, J. Phys. Chem. B 108 (2004) 17886–17892.

[24] G. Li, B. Zou, S. Feng, H. Shi, K. Liao, Y. Wang, W. Wang, G. Zhang, Synthesis of N-doped TiO$_2$ with good photocatalytic property, Phys. B 588 (2020) 412184–412189.

[25] Y. Cong, J. Zhang, F. Chen, M. Anpo, Synthesis and characterization of nitrogen-doped TiO$_2$ nanophotocatalyst with high visible light activity, J. Phys. Chem. C 111 (2007) 6976–6982.

[26] F. Zhou, H. Song, H. Wang, S. Komarneni, C. Yan, N-doped TiO$_2$/sepiolite nanocomposites with enhanced visible-light catalysis: role of N precursors, Appl. Clay Sci. 166 (2018) 9–17.

[27] A. Sanchez-Martinez, O. Ceballos-Sanchez, C. Koop-Santa, E.R. López-Mena, E. Orozco-Guareño, N-doped TiO$_2$ nanoparticles obtained by a facile coprecipitation method at low temperature, Ceram. Int. 44 (2018) 5273–5283.

[28] X. Lei, Z. Shi, X. Wang, T. Wang, J. Ai, P. Shi, R. Xue, H. Guo, W. Yang, Solvothermal synthesis of pompon-like nickel-cobalt hydroxide/graphene oxide composite for high-performance supercapacitor application, Colloids Surf. A 549 (2018) 76–85.

[29] P.R. Jothi, S. Kannan, G. Velayutham, Enhanced methanol electro-oxidation over in-situ carbon and graphene supported one dimensional NiMoO$_4$ nanorods, J. Power Sources 277 (2015) 350–359.

[30] W. Huang, Z. Li, Y. Peng, S. Chen, J. Zheng, Z. Niu, Oscillatory electrocatalytic oxidation of methanol on an Ni(OH)$_2$ film electrode, J. Solid State Electrochem. 9 (2005) 284–289.

[31] X. Lu, Y. Bai, R. Wang, J. Sun, A high-performance flexible and weavable asymmetric fiber-shaped solid-state supercapacitor enhanced by surface modifications of carbon fibers with carbon nanotubes, J. Mater. Chem. A 4 (2016) 18164–18173.

[32] A.A. Dubale, Y. Zheng, H. Wang, R. Hübner, Y. Li, J. Yang, J. Zhang, N.K. Sethi, L. He, Z. Zheng, High-performance bismuth-doped nickel aerogel electrocatalyst for the methanol oxidation reaction, Angew. Chem. Int. Ed. 59 (2020) 13891–13899.

[33] I. Hod, P. Deria, W. Bury, J.E. Mondloch, C.-W. Kung, M. So, M.D. Sampson, A. W. Peters, C.P. Kubiak, O.K. Farha, A porous proton-relaying metal-organic framework material that accelerates electrochemical hydrogen evolution, Nat. Commun. 6 (2015) 8304–8313.

[34] Y. Dou, S. Zhang, T. Pan, S. Xu, A. Zhou, M. Pu, H. Yan, J. Han, M. Wei, D.G. Evans, TiO$_2$@Layered double hydroxide core–shell nanospheres with largely enhanced photocatalytic activity toward O$_2$ generation, Adv. Funct. Mater. 25 (2015) 2243–2249.

[35] W. Song, X. Teng, Y. Liu, J. Wang, Y. Niu, X. He, C. Zhang, Z. Chen, Rational construction of self-supported triangle-like MOF-derived hollow (Ni, Co)Se$_2$ arrays for electrocatalysis and supercapacitors, Nanoscale 11 (2019) 6401–6409.

[36] M.C. Biesinger, B.P. Payne, A.P. Grosvenor, L.W. Lau, A.R. Gerson, R.S.C. Smart, Resolving surface chemical states in XPS analysis of first row transition metals, oxides and hydroxides: Cr, Mn, Fe, Co and Ni, Appl. Surf. Sci. 257 (2011) 2717–2730.

[37] B. Tudu, N. Nalajala, P. Saikia, C.S. Gopinath, Cu–Ni bimetal integrated TiO$_2$ thin film for enhanced solar hydrogen generation, Sol. RRL 4 (2020) 1900557–1900567.

[38] H. Onishi, T. Aruga, C. Egawa, Y. Iwasawa, Photoelectron spectroscopic study of clean and CO adsorbed Ni/TiO$_2$ (110) interfaces, Surf. Sci. 233 (1990) 261–268.

[39] A. Panepinto, D. Cornil, P. Guttmann, C. Bittencourt, J. Cornil, R. Snyders, Fine control of the chemistry of nitrogen doping in TiO$_2$: a joint experimental and theoretical study, J. Phys. Chem. C 124 (2020) 17401–17412.

[40] Z. Wu, Y. Zhao, W. Jin, B. Jia, J. Wang, T. Ma, Recent progress of vacancy engineering for electrochemical energy conversion related applications, Adv. Funct. Mater. 31 (2021) 2009070–20090106.

[41] N.A. Barakat, M. Motlak, CoxNiy-decorated graphene as novel, stable and super effective non-precious electro-catalyst for methanol oxidation, Appl. Catal., B 154 (2014) 221–231.

[42] M. Zhu, C. Zhai, M. Sun, Y. Hu, B. Yan, Y. Du, Ultrathin graphitic C$_3$N$_4$ nanosheet as a promising visible-light-activated support for boosting photoelectrocatalytic methanol oxidation, Appl. Catal. B 203 (2017) 108–115.

[43] E. Antolini, Photo-assisted methanol oxidation on Pt-TiO$_2$ catalysts for direct methanol fuel cells: a short review, Appl. Catal. B 237 (2018) 491–503.

[44] Y. Kang, B. Jiang, J. Yang, Z. Wan, J. Na, Q. Li, H. Li, J. Henzie, Y. Sakka, Y. Yamauchi, Amorphous alloy architectures in pore walls: mesoporous amorphous NiCoB alloy spheres with controlled compositions via a chemical reduction, ACS Nano 14 (2020) 17224–17232.

[45] F. Wu, Z. Zhang, F. Zhang, D. Duan, Y. Li, G. Wei, S. Liu, Q. Yuan, E. Wang, X. Hao, Exploring the role of cobalt in promoting the electroactivity of amorphous Ni-B nanoparticles toward methanol oxidation, Electrochim. Acta 287 (2018) 115–123.

[46] P. Petersen, W. Krasser, Surface enhanced Raman scattering from a ternary catalyst Cu/ZnO/Al$_2$O$_3$ under reaction conditions, Appl. Surf. Sci. 103 (1996) 91–100.

[47] W. Shan, R. Liu, H. Zhao, Z. He, Y. Lai, S. Li, G. He, J. Liu, In situ surface-enhanced raman spectroscopic evidence on the origin of selectivity in CO$_2$ electrocatalytic reduction, ACS Nano 14 (2020) 11363–11372.

[48] D. Adams, S. Payne, K. Martin, The fluorescence of diamond and Raman spectroscopy at high pressures using a new design of diamond anvil cell, Appl. Spectrosc. 27 (1973) 377–381.